

The Milky Way as Seen by Classical Cepheids II: Spiral Structure

Drimmel, R.¹, Khanna, S.¹, Poggio, E.¹, and Skowron, D. M.²

¹ INAF - Osservatorio Astrofisico di Torino, via Osservatorio 20, 10025 Pino Torinese (TO), Italy
e-mail: ronald.drimmel@inaf.it

² Astronomical Observatory, University of Warsaw, Al. Ujazdowskie 4, 00-478 Warsaw, Poland

Received ; accepted

ABSTRACT

As a relatively young and bright population, and the archetype of standard candles, classical Cepheids make an ideal population to trace non-axisymmetric structure in the young stellar disk to large distances. We use the new distances derived in Paper I based on mid-IR WISE photometry for a selected sample of 2857 dynamically young Cepheids to trace the spiral arms of the Milky Way. The Perseus and Sagittarius-Carina arms are clearly evident in the third and fourth Galactic quadrants, while the Local and Scutum arms are much weaker, with extinction severely limiting our view of the latter, inner-most spiral arm. Pitch angles are derived for each arm over various ranges of galactic azimuth, each covering at least 90° in azimuth. Our method of detecting spiral arms and deriving pitch angles does not rely on pre-assigning sources to specific arms. While spiral structure in the first and second quadrant is not obvious, in part due to extinction effects, it is not inconsistent with that seen in the third and fourth quadrants. In summary, the Cepheids allow us to map spiral structure in the third and fourth galactic quadrants where there are currently few masers with astrometric parallaxes, thus significantly extending our picture of the Milky Way on large-scales.

Key words. Galaxy: kinematics and dynamics – Galaxy: structure – Galaxy: disc – Stars: variables: Cepheids

1. Introduction

Mapping the large-scale spiral structure of the Milky Way, as traced by star formation, has been a perpetual challenge due to our location within a dust-filled disk. In the optical we are limited to about four to five kiloparsecs from the Sun using bright young stars as seen by *Gaia* (Xu et al. 2018; Zari et al. 2021; Poggio et al. 2021; Gaia Collaboration et al. 2022, hereafter GD22). Thanks to the absolute astrometry of maser radio sources, identified as being high-mass stars hosting circumstellar disks, major progress has been made in the past decade mapping the first and second galactic quadrants (Reid et al. 2019; VERA Collaboration et al. 2020). However, the number of masers with measured parallaxes in the third and fourth quadrants, visible mostly from the southern hemisphere, is still quite limited and does not provide sufficient sources to confidently map the location of the star-formation complexes that are responsible for the spiral structure that we would see in the optical. For a recent review attempting to integrate the *Gaia* astrometry for young stars and the data from radio masers see Xu et al. (2023).

In this work we investigate the spiral structure as seen by Classical Cepheids, a predominantly young population of stars whose distances can be reliably found thanks to them being the archetype of the standard candle. Previous studies of spiral structure using Cepheids include Griv et al. (2017), who used 674 Cepheids within about 3kpc, and identified three arm segments with pitch angles of 12, 10, 17°, using a "Fourier" decomposition of three log-spiral components. Skowron et al. (2019a,b) showed that the distribution of 2390 Cepheids in the Galactic plane is consistent with the majority being born in spiral arms, once diffusion effects and the radial age-gradient of the Cepheids is taken into account. However, no attempt was made to map or parameterize the spiral arms themselves. Meanwhile, Min-

niti et al. (2021) used 50 Classical Cepheids in a first attempt to model the spiral arms on the far side of the Galaxy.

More recent attempts to map spiral structure with the Classical Cepheids of the Milky Way include Lemasle et al. (2022) who used a sample of 2684 Cepheids compiled from various variability catalogues, with distances derived using a period-Wesenheit relation in the WISE bands and *Gaia* parallaxes for Cepheids with no unWISE photometry. Using primarily the subsample of Cepheids younger than 150 Myr they identify numerous spiral arm segments. Meanwhile Bobylev (2022) used about 600 pre-selected Cepheids from Skowron et al. (2019a,b) to measure the pitch angle of the Sgr-Car arm and an outer arm beyond Perseus. GD22 used 2808 young classical Cepheids to construct an overdensity map of the Cepheids, identifying the Sagittarius and Perseus arms, but making no attempt to parameterize the arms.

The identification of the Cepheids are dependent on observations made in the optical where their variability follows a characteristic profile needed for identification. Our distances instead rely on *W1* mid-infrared (midIR) photometry from the WISE satellite (Wright et al. 2010). Relying on midIR photometry both minimizes the effect of extinction, which must be taken into account when deriving the photometric distances, as well as minimizing the uncertainty from the intrinsic scatter about the PL relation (Bono et al. 2024). Rather than using Wesenheit-based distances, in this work we use the recent Cepheid distances derived from WISE midIR *W1* photometry that rely on the PL relation in *W1* and an extinction model (Skowron et al. 2024, submitted, hereafter Paper I). A comparison between these and Wesenheit-based distances show systematic differences toward the inner disk of the Milky Way that can be attributed to unaccounted for variations of the extinction curve. These new distances were val-

idated on a set of 910 Cepheids with good astrometry and shown to have relative distance uncertainties smaller than 13%.

The paper is organised as follows: Section 2 describes our selection of young Cepheids to be used as spiral tracers, and section 3 our method of identifying and characterising spiral arms in the distribution of our sample. In section 4 we present the results of our analysis over various ranges of galactic azimuth angle, as well as consider alternative age selection criteria. Finally in section 5 we discuss our results in the context of past efforts to map the Galactic spiral structure on large scales, and in section 6 we briefly summarize our results.

2. Data

To trace the young population we use the sample of 3659 known Classical Cepheids from Pietrukowicz et al. (2021), for which we have derived new distances for 3425 Cepheids based on WISE *W1* photometry from AllWISE (Cutri et al. 2013) and unWISE (Schlafly et al. 2019) in Paper I. For details on the definition of the sample and the derivation of their distances the reader is referred to Paper I.

Finally, from this catalogue of Cepheid distances we remove those whose distances are clearly inconsistent with their astrometry, namely using the quantity provided in the catalogue

$$Q = |\Delta\varpi/\sigma_{\Delta\varpi}|, \quad (1)$$

where $\Delta\varpi = \varpi - \varpi_\mu$, ϖ_μ being the photometric parallax for a source with a distance modulus μ , that is,

$$\varpi_\mu = 10^{-(\mu-10)/5}, \quad (2)$$

and $\sigma_{\Delta\varpi}$ the estimated uncertainty of $\Delta\varpi$. (See Paper I for details.) We impose the condition that $Q < 5$. This removes 63 presumable contaminants from our sample, leaving a total of 3362 Cepheids.

2.1. Cepheid age selection

For age estimates of our sample of Cepheids we use the ages provided in Paper I, based on the period-age-metallicity relationship derived by Anderson et al. (2016), who take into account the effect of rotation. (See Paper I for further details.) While these ages may be quite uncertain for individual Cepheids, we assume that they are sufficiently accurate to make a sample selection.

Since Cepheids can span a significant range of ages, but we wish to use them as a tracer of a young stellar population, we will want to make an age selection. Common age cuts found in the literature for this purpose are typically 200 Myr or younger. However, because of the metallicity gradient, Cepheids in the outer Galaxy are systematically older than those in the inner Galaxy, as low-mass stars in metal-rich environments do not reach the Cepheid instability strip during their evolution (Skowron et al. 2019a; Anders et al. 2024). As a result, a simple age selection will exclude many Cepheids in the outer disk. In addition, such an age cut does not take into account that dynamical timescales are very different in the outer Galaxy with respect to the inner Galaxy. Indeed, Cepheids as old as 200 Myr or more may still not have had time to wander far from their radius of birth in the outer Galaxy, while Cepheids of the same age in the inner Galaxy may have already completed nearly two galactic rotations.

As an alternative to a simple age cut, we make a selection based on the dynamical age of the Cepheids, that is, their age with respect to the epicyclic frequency at their current galactocentric radius. We thus require their age to be less than the

epicyclic period ($= 2\pi/\kappa$), where in the epicyclic approximation the epicyclic frequency κ is:

$$\kappa^2(R_g) = \left(R \frac{d\Omega^2}{dR} + 4\Omega^2 \right)_{R_g}, \quad (3)$$

where R is the Galactocentric cylindrical radius, and the angular velocity $\Omega^2 = V_\phi^2/R^2$. Evaluating Ω^2 at the guiding radius R_g we can substitute $\Omega(R_g)^2 = L_Z^2/R_g^4$, where L_Z is the vertical angular momentum component. In Drimmel et al. (2023) we showed that the angular momentum L_Z of the subset of DR3 Cepheids with line-of-sight velocities followed a simple linear relation with respect to Galactocentric radius R , that is $L_Z(R) = 231.4 \text{ km s}^{-1}R$, over a range of radii $5 < R < 18 \text{ kpc}$, implying a flat rotation curve of 231.4 km s^{-1} over this radial extent. Taking L_Z as a proxy for R_g , we thus find $\Omega(R_g) = 231.4/R_g$ for the angular velocity of the Cepheids, and the epicyclic frequency is then $\kappa(R_g) = \sqrt{2} \cdot 231.4/R_g$. Making the further assumption that the guiding radius R_g can be substituted by R (approximately true for a genuinely young population), our age criteria becomes

$$\text{Age}_{\text{Myr}} < \frac{\sqrt{2}\pi R}{0.2314}, \quad (4)$$

for R in kpc and using the convenient approximation $1 \text{ km s}^{-1} \approx 1 \text{ pc per Myr}$. At the solar radius this requires Cepheids to be younger than about 160 Myr to be considered dynamically young. A more accurate determination of R_g per star would require that line-of-sight velocities are available.

To apply the above criteria (Eq. 4), we just need the Galactocentric cylindrical radius R , which we derive using ESO Gravity project's most recent derivation of the Sun's distance from the Galactic center, R_\odot , based on the measurements of stars orbiting the Milky Way's supermassive black hole Sgr A*, namely $R_\odot = 8277 \pm 9(\text{stat}) \pm 30(\text{sys}) \text{ pc}$ (GRAVITY Collaboration et al. 2022). Heliocentric Cartesian coordinates are defined by

$$\begin{pmatrix} x \\ y \\ z \end{pmatrix} = \begin{pmatrix} d \cos l \cos b \\ d \sin l \cos b \\ d \sin b \end{pmatrix}, \quad (5)$$

for galactic coordinates (l, b) and a heliocentric distance d . We translate to galactocentric Cartesian coordinates (X, Y, Z) using R_\odot and, for simplicity, assuming $Z_\odot = 0$, keeping the X axis pointing in the direction of the Galactic Center as seen from the Sun. That is, $X = x - R_\odot$, $Y = y$ and $Z = z$. The galactocentric cylindrical radius R is then $\sqrt{X^2 + Y^2}$, and Galactocentric azimuth is taken as $\phi = \tan^{-1}(Y/X)$. Note that galactocentric azimuth defined in this way increases in the anti-clockwise direction, while the rotation of the Galaxy is clockwise, as seen from the north Galactic pole.

Fig. 1 shows the age of the Cepheids with respect to galactocentric radius and our age selection. The dynamically young criteria becomes a more stringent cut as we move to smaller galactocentric radii, but the mean age gradient of Cepheids mentioned above results in most Cepheids being dynamically young in any case. In contrast, in the outer Galaxy, our new age criteria allows us to include many Cepheids that would otherwise be excluded from our sample if we were to use a simple age criteria. Indeed, 374 of our 2857 dynamically young Cepheids are older than 200 Myr.

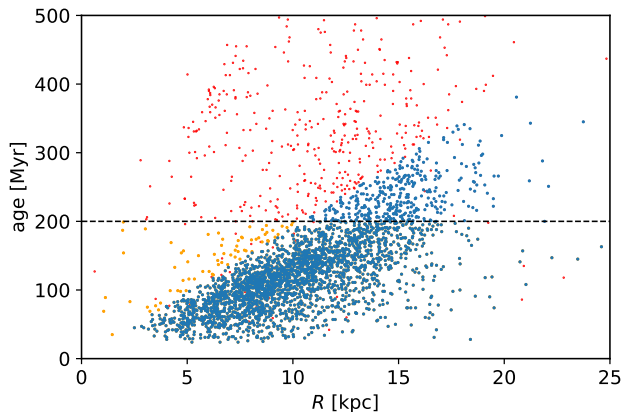


Fig. 1. Distribution of Cepheid ages with respect to Galactocentric radius. Blue points are the dynamically young Cepheids, yellow points the Cepheids that are younger than 200 Myr but not dynamically young, while red points are Cepheids older than 200 Myr that are also not dynamically young.

3. Identification and characterisation of spiral arms

We now use the dynamically young Cepheids to map the spiral arms. Fig. 2 shows the positions of the dynamically young Cepheids in the Galactic plane, in galactocentric coordinates, where one can see a spiral arm clearly traced by the Cepheids in the fourth quadrant ($270^\circ < l < 360^\circ$), just inside the Sun's position. As this arm can be clearly traced from $l = 0^\circ$ (Sagittarius) to the arm tangent in the direction of Carina ($l \approx 285^\circ$), we will identify this arm as the Sagittarius-Carina (Sgr-Car) arm. Another weaker and broader arm is also somewhat visible in the third quadrant ($180^\circ < l < 270^\circ$). Meanwhile in the first and second quadrant the distribution of the Cepheids does not show obvious spiral structure, but is much more discontinuous and "patchy". The lack of obvious spiral features in the first and second quadrants is in part due to the non-uniform coverage in this half of the Galaxy due to interstellar extinction, which introduces gaps or "shadow cones" along lines-of-sight with strong foreground extinction. Some of these shadow cones are easily recognised in Fig. 2, in particular one in the direction of $l \approx 80^\circ$ starting at about 2-3 kpc from the Sun, where the Cygnus X star forming region is located. Extinction has a greater affect in the first and second quadrants in part due to the geometry of the spiral arms: In these directions our lines-of-sight crosses spiral arms in closer vicinity than in the third and fourth quadrant where the separation of the arms is increasing, allowing us an unhindered view over larger ranges in galactic longitude. The dust lanes of a spiral arm can limit the view of the arm itself, as well as any other arms beyond it. However, not all the "patchiness" can be explained by extinction, but is also to some extent due to the fact that star formation itself is patchy, and does not occur continuously along spiral arms. Finally, we should not forget that our sample, being based on a set inhomogeneous catalogues, has a selection function that is a sum result of overlapping surveys covering different parts of the sky (see Paper I for further details). In any case, for the purpose of this study, we will mostly limit ourselves to the study of the orientation of the spiral arms over large scales, as seen in the distribution of the Cepheids.

We now reconsider the spatial distribution of the Cepheids in the $\ln R/R_\odot$ and ϕ' plane (see Fig. 3), where $\phi' = \pi - \phi$ in radians, so that $\phi' = 0$ is in the direction of the galactic anticenter, and is positive in the direction of galactic rotation. In

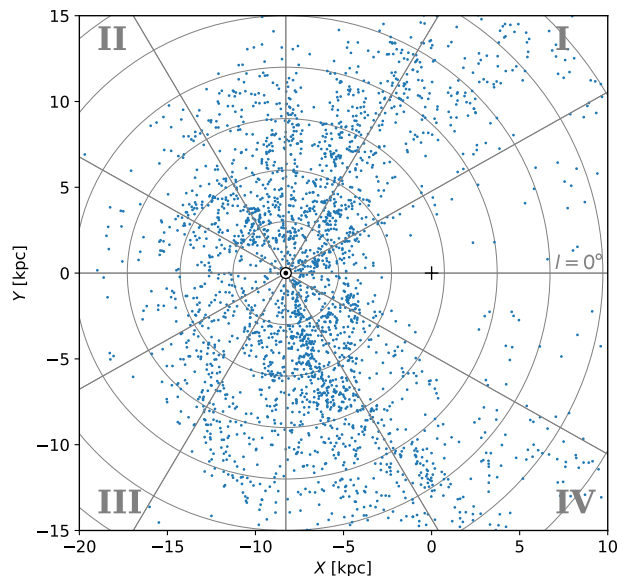


Fig. 2. Distribution of 2857 dynamically young Cepheids in the Galactic plane. Dark blue points are the positions of the dynamically young Cepheids. The positions of the Galactic center (+) and the Sun (\odot) are indicated, and the overlaying polar grid shows galactic longitude in 30° intervals and heliocentric distances at 3 kpc intervals. The Galactic quadrants are indicated with Roman numerals.

these coordinates logarithmic spiral arms should appear as linear features with negative slopes. Indeed, for $\phi' < 0$ (the third and fourth Galactic quadrants), two such linear features are readily apparent, but not for $\phi' > 0$ (the first and second Galactic quadrants). To confirm and measure in a quantifiable way the orientation (pitch angle) of any spiral arms that might be traced by the Cepheids, we consider a range of possible pitch angles. We define the rotated coordinate in the $\ln(R/R_\odot) - \phi'$ plane:

$$y' = \ln(R/R_\odot) \cos \theta + \phi' \sin \theta, \quad (6)$$

where the angle θ corresponds to an assumed pitch angle, and $y' = 0$ is the y' position of the Sun. If a spiral arm is present then we expect that the distribution of Cepheids in y' to present a clear peak at the position of the arm when θ corresponds to the actual pitch angle of the arm. As we deviate from the correct pitch angle for an arm, the peak in the y' distribution will become broader and less prominent.

As an example we show in Fig. 4 the y' distribution of 1431 dynamically young Cepheids in the ϕ' range $[-120^\circ, 0^\circ]$ (corresponding to $180^\circ < \phi < 300^\circ$) for an assumed pitch angle of 15° . Three clear peaks are seen in the distribution, one inside the Sun's position ($y' < 0$) and two outside the Sun's position. We identify and measure the position of the peaks by first performing a KDE density estimate using a Gaussian kernel (here using a bandwidth of 0.025), as implemented in the KernelDensity function from the Python SKLEARN package Pedregosa et al. (2011). This density is then used as input to the Python scipy.signal.find_peaks function, requiring a minimum peak width of 0.05 (in y') and a minimum peak prominence (i.e. height) of 0.2. The find_peaks function identifies the position of the peaks, and gives a measure of the peak prominence and peak width, which is evaluated at half of the relative peak height.

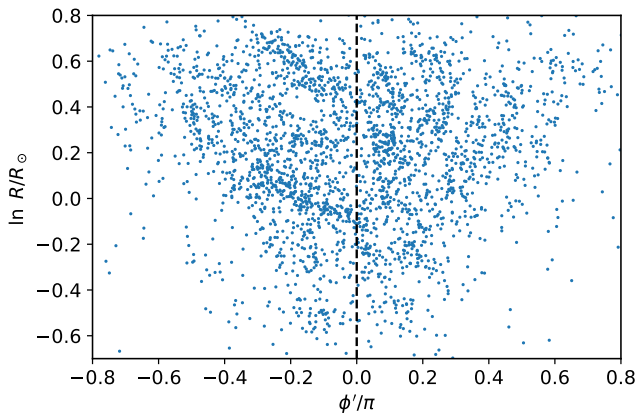


Fig. 3. Distribution of dynamically young Cepheids in the $\ln R/R_\odot$ (natural log) and ϕ' , where $\phi' = 0$ is in the direction of the galactic anticenter and in radians.

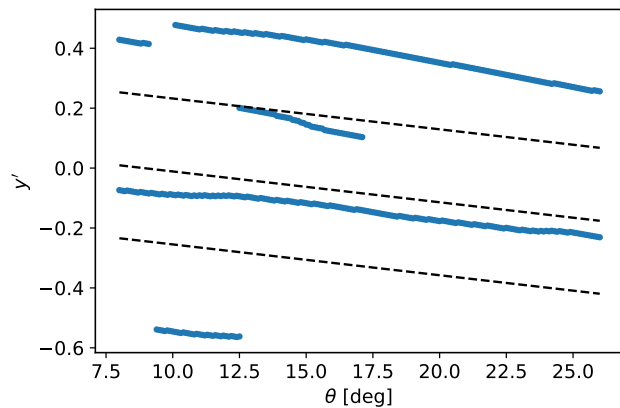


Fig. 5. Position of the detected peaks for assumed pitch angles of $8 < \theta < 28^\circ$ for the Cepheids with azimuths $-120^\circ < \phi' < 0^\circ$. Dashed lines show the boundaries used to assign peak properties to specific putative arms.

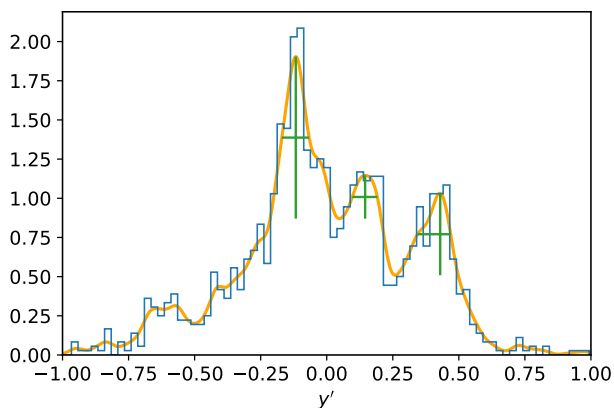


Fig. 4. Distribution of dynamically young Cepheids in y' for an assumed pitch angle of 15° for the sample between azimuths $-120^\circ < \phi' < 0^\circ$. The orange curve is the KDE density for a bandwidth of 0.025. The three identified peaks are indicated by their measured prominence (vertical green lines) and widths (horizontal green lines).

Depending on the azimuth range and assumed pitch angle, the number of peaks ranges from two to four, with generally one or two arms found within the Sun's position. The position of the peaks are used to assign the peak properties (peak prominence and strength) to a putative arm. The first arm (at $y' \approx -0.15$ in Fig. 5), inside the Sun's position, which we have already identified above as the Sgr-Car arm, is always detected, except for assumed pitch angles $\theta > 22^\circ$ for the ϕ' range $[-30^\circ, 60^\circ]$. Another ubiquitous arm is the Perseus arm, the outer-most arm detected outside the Sun's position. The identification of this arm is based on it going through a large group of Cepheids about 2-3.5 kpc away between galactic longitudes $110^\circ < l < 150^\circ$ when extrapolated into the second quadrant, an area with active star formation that has long been identified as the Perseus arm (Morgan et al. 1953; van de Hulst et al. 1954). More recently it has been also mapped and identified as the Perseus arm with masers by Reid et al. (2019, hereafter R19), and in ionized gas by Haffner et al. (1999).

There are two other arms that are sporadically detected, one inside the Sgr-Car arm which we tentatively identify as the Scutum arm based on its distance toward the Galactic Center, and

one just outside the Sun's position but closer than the Perseus arm, which we identify as the Local or Orion arm. We will discuss in more detail the geometry and identification of the arms in Section 5.

Since we expect peaks corresponding to a spiral arm to be most prominent and narrowest when the angle θ corresponds to the actual pitch angle of the arm, we define the quantity $strength = prominence/width$. As the distribution in azimuth of our sample is not centered at $\phi' = 0$, we find that the peak positions will in general "drift" to smaller y' values as the angle θ is increased. Fig. 5 shows, for the dynamically young Cepheids in the ϕ' range $[-120^\circ, 0^\circ]$, the position of the detected peaks as we consider possible pitch angles between 8° and 26° in steps of 0.1° . The dashed lines show the boundary criteria used to assign the peak properties to specific arms. Any peaks above/below the upper/lower boundaries are assigned to outer/inner-most arms, allowing for the detection of up to four arms. The boundary between the outer and inner arms (middle dashed line) is

$$y'_b = 0.4 (\langle \ln(R/R_\odot) \rangle \cos \theta + \langle \phi' \rangle \sin \theta) - 0.3 \theta \quad (7)$$

where the quantities between the $\langle \rangle$ brackets are the median values of the sample selected, and θ is in radians. The first term sets the vertical offset in y' , while the second term primarily determines the slope of the lines. The coefficients 0.4 and 0.3 were found by trial and error, checking that it was sufficient for all the different azimuth ranges considered. The other two boundaries are set at $\pm \Delta y'$ from y'_b , the half distance between the outermost peak and the first peak inside the Sun's position, that is the peaks corresponding to the Perseus and Sgr-Car arms. In the infrequent case that no outer peak is detected, the default interval in $\Delta y' = 0.25$ is used.

Once the peak properties are assigned to each arm for different possible pitch angles θ , we find the angles at which the peak prominence and peak strength is maximum, taking the angles of the maximum as the pitch angle of the arm. This gives us two possible pitch angles for each arm. While for most azimuth ranges and data selections there is only one clear peak over the range of possible pitch angles considered, Fig. 6 shows that it may occur that the peak strength shows two maxima. This behaviour in the peak strength is in part due to the strength being more sensitive to weaker but narrower peaks in the y' distribution. In any case, the primary peak in the peak strength for the

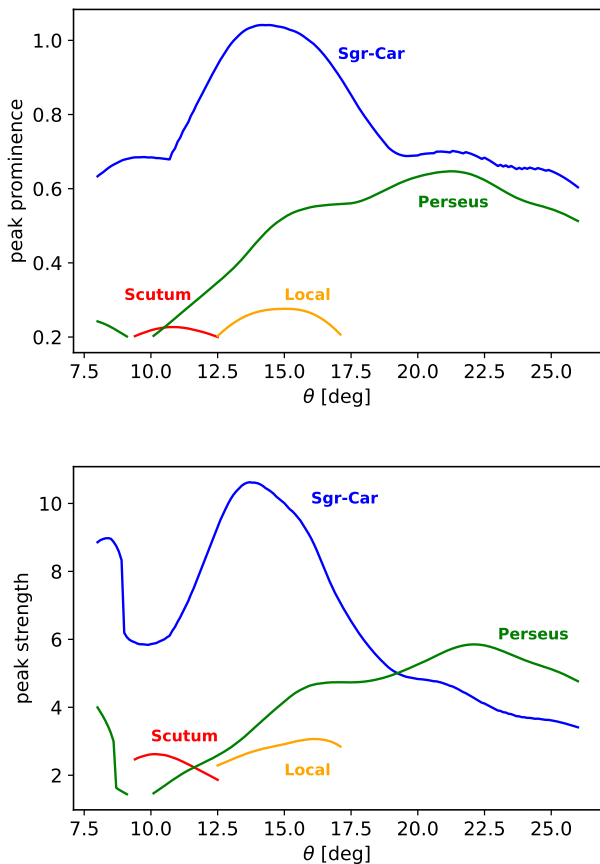


Fig. 6. Variation of the prominence and strength of the peaks with respect to the assumed pitch angle θ for the Cepheids with azimuths $-120^\circ < \phi' < 0^\circ$. The blue curve is for the first arm inside the Sun's position (Sgr-Car), the gold curve the first arm outside the Sun's position (the "local" Orion arm), and the green curve for the furthest arm detected.

Sgr-Car occurs at nearly the same pitch angle θ as that seen in the peak prominence.

In summary, for the data selection used in this section – dynamically young Cepheids over the ϕ' azimuth range of $[-120^\circ, 0^\circ]$ – we find pitch angles of 10.7, 14.2, 15 and 21.3° for the four detected arms when considering the peak prominence, and 10.1, 13.7, 16.1, 22.1° for the peak strength. As can be seen in Fig. 6, the Scutum and Local (Orion) arm are quite weak with respect to the Sgr-Car and Perseus arms. Nevertheless, the estimated pitch angles fall within a couple of degrees of each other for all the arms. We also note that there is an increase in the pitch angles of the arms as we move outward from the Galactic center.

Once a pitch angle for an arm is found, we can find the position of the arm using the y' position of the peak at that pitch angle in equation 6, taking $\phi' = 0$ and solving for $\ln(R)_{\phi'=0}$, which we designate as $\ln(R_0)$. A spiral arm described by the equation

$$R = R_0 e^{-\tan \theta \phi'} \quad (8)$$

then corresponds to the equation

$$\ln(R/R_\odot) = \ln(R_0/R_\odot) - \phi' \tan \theta. \quad (9)$$

Using the equation above, we can over plot the derived position of the arms on the $\ln R$ – ϕ' distribution, as shown in Fig. 7.) Each

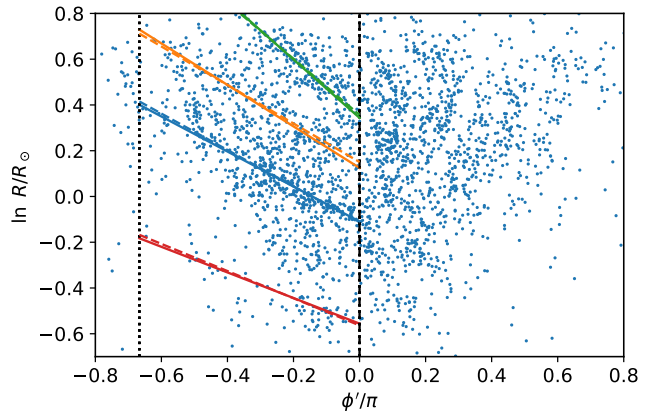


Fig. 7. Distribution of young DR3 Cepheids in $\log R/R_\odot$ and ϕ' , as in Fig. 3, but with the positions of the arms overplotted derived using the Cepheids with azimuths $-120^\circ < \phi' < 0^\circ$. Red corresponds to the Scutum arm, blue to the Sgr-Car arm, orange the local Orion arm, and green the outermost (Perseus) arm. Solid (dashed) lines show the arms using the pitch angles found from the maximum strength (prominence).

spiral arm is thus characterised by two parameters, the pitch angle θ and $\ln(R_0)$, derived from the pitch angle and the measured y' position of the peaks.

We estimate the uncertainty of the measured peak positions by performing a bootstrap of $N = 100$ samples of the y' distribution. Using the standard deviation of the peak positions, we find that the uncertainty of the peak positions for the three detected arms (at $\theta = 15^\circ$ and for the sample Cepheids between $-120^\circ < \phi' < 0^\circ$, shown in Fig. 4) to be 0.005, 0.019 and 0.017, showing that the peak positions are well determined. The same bootstrapping technique can also be used to test the robustness of the detection of each arm. For instance, at the pitch angle of $\theta = 15^\circ$ the Sgr-Car and Perseus arm is found in all 100 bootstraps, while the Local (Orion) arm is only detected 86% of the time. Rerunning this procedure for a pitch angle of $\theta = 11^\circ$ to allow us to detect the Scutum arm, gives us uncertainties in the y' positions of the peaks of 0.026, 0.009, 0.048 and 0.028. Again, for 100 bootstraps the Sgr-Car arm is always detected, while the detection rates for the Scutum arm is 74%, for the Local arm is only 41%, and that of the Perseus arm is 88%. That the Perseus arm is not always detected at this small pitch angle is not surprising, while the sporadic detection of the Scutum and Orion arms, even at an angle θ near their pitch angles indicates how weak they are, at least in this dataset.

The resulting uncertainties of the determined pitch angles are more difficult to estimate because it depends on the variation of the y' distribution as we vary θ , which is determined by a given set of measured Cepheid positions in the Galactic plane. The uncertainty of these positions are in turn a consequence of our distance uncertainties. We generate alternative sets of measured Cepheid positions by assuming that the distance uncertainties are well described by a Gaussian distribution in the distance modulus of each Cepheid with a standard deviation of σ_μ , the uncertainty in the distance modulus. In this way we generate 100 samples from our dataset. We analyse each sample as described above, identifying the peaks in the y' coordinate for a range of possible pitch angles, measuring their prominence and strength, and identifying the pitch angle for each arm for which these properties are maximum. We take the standard deviation of our 100 determinations of the pitch angle for each arm as an esti-

mate of the uncertainty of the pitch angle. Using the peak prominence we find uncertainties of 1.0, 0.7, 1.7, 1.4° for the Scutum, Sgr-Car, Orion and Perseus arms respectively. Similarly, using the peak strength we find uncertainties of 1.2, 1.4, 1.8, 3.2°. Not unexpectedly, the estimated pitch angles from the two methods agree with each other within the uncertainties.

From the same 100 samples we can also measure the robustness of the detection of each arm, similarly as was done above when bootstrapping the y' distribution for our dataset. We find that the Sgr-Car and Perseus arms are detected in 100% of the resamples, the Local (Orion) arm in 74%, and the Scutum arm in only 32% of the resamples.

4. Results

In the previous section we described our method using as an example the 1431 dynamically young Cepheids with azimuths $-120^\circ < \phi' < 0^\circ$. In this section we consider alternative selected azimuth ranges to explore the possible extent of each arm as well as possible variation of the pitch angles. We also discuss the effect of alternative age selections.

We always explore azimuth ranges that are at least 90° in extent, and that start at azimuths $\phi' < 60^\circ$ ($\phi > 120^\circ$). Azimuths at $\phi' > 60^\circ$ are not considered due to the lack of data in the inner disk as a consequence of extinction, which limits how far we can trace the arms into the first quadrant. For all the azimuth ranges considered we will use the same scheme as in the previous section for identifying the arms: the first arm within the Sun's position we identify as Sgr-Car, and the outermost arm as Perseus. Table 1 summarizes our results for each arm for the different azimuth ranges considered, listing the different azimuth ranges, the number of Cepheids found in each azimuth range, and the spiral arm parameters found using either the peak prominence or peak strength.

We overplot all of the spiral arm fits in Fig. 8 for all the azimuth ranges on the Galactocentric XY positions of the Cepheids, using equation 8. In general the positions of the arms at $\phi' = 0$ ($\ln R_0$) are very consistent for all the arms, across all the azimuth ranges considered, regardless of whether using the strength or prominence of the arm to estimate the arm parameters. The coincidence of the positions of the arms found for the different azimuth ranges confirms that we are indeed seeing the same arm, using the position of the peaks in y' -space with respect to the Sun to identify the arms. The pitch angles of the arms are also fairly consistent for all the azimuth ranges, with the exception of the Local (Orion) arm showing larger pitch angles when data from the first and second quadrants ($\phi' > 0.$) are included, increasing from 15° (similar to the Sgr-Car arm) to 22° (similar to the Perseus arm). The pitch angles of the Perseus arm are quite consistent between the two methods, with a very gradual progression from 22° to 20° as we take azimuth ranges moving from negative to positive ϕ' , except for the azimuth range $[-30^\circ, 60^\circ]$ where the two methods diverge. The pitch angle of the Sgr-Car arm is more consistent over the azimuth ranges considered, with the pitch angles from the arm strength being consistently a bit smaller than those from the arm prominence. Indeed, the spiral arms overplotted for all the arms nearly overlap each other, with the Local (Orion) arm showing the most variation in pitch angle when different azimuth ranges are considered.

In general the pitch angles of the arms are not the same, but increase as we move outward from the inner to the outer Galaxy, from about 10° for the Scutum arm to about 20 - 22° for the Perseus arm. This trend, noted in the previous section, is preserved for all azimuth ranges considered.

Apparently, though the Cepheids in the first and second quadrants do not show obvious spiral arm structure, the clumpy distribution of the Cepheids is not inconsistent with the assumption that the spiral structure seen in the third and fourth quadrants extends into the first and second quadrants, at least for the three outermost arms. In contrast, the innermost Scutum arm is not detected when data from the first and second quadrants is considered. Indeed, the detection of this arm is quite weak, and we can at most claim a tentative detection of the Scutum arm. The Local (Orion) arm on the other hand is detected at all azimuth ranges, though it is always weak relative to the Sgr-Car and Perseus arms.

As the individual ages are very uncertain, we explore the effect of alternative age selections. First, we repeat the analysis for all the azimuth ranges with the selection

$$Age_{Myr} < \frac{\pi R}{0.2314}, \quad (10)$$

that is, requiring the Cepheids to be younger than half the dynamical time (Galactic rotation period) at their current galactocentric radius. This is a more stringent selection than used above, reducing our sample to 1894 Cepheids. With such a selection we still have sufficient Cepheids in the inner disk, but we lose most of Cepheids in the outer disk, thus losing most of the advantage of using a dynamical age selection. As a consequence our detection of the outer (Perseus) arm is much weaker. Nevertheless, it is still detected with pitch angles similar to those reported above, notwithstanding that the peaks in the strength and prominence are much less pronounced. The Local (Orion) arm is also still detected, but shows a larger variation of pitch angles, with larger systematic differences between the two methods. The Sgr-Car arm remains easily detected, while the Scutum arm is just barely detected, but both arms have similar pitch angles as reported above.

If instead we impose a simple age cut of $Age_{Myr} < 200$ Myr, then the Perseus arm is only very weakly detected for the two azimuth ranges restricted to the 3rd and 4th quadrant, with no clear peak with respect to pitch angle in either the arm strength or prominence, while the Local (Orion) arm is no longer detected. For the other azimuth ranges that include Cepheids in the first and second quadrant, both arms show the same trends in pitch angles as reported above. Meanwhile the Sgr-Car and Scutum arms are unaffected, and show the same pitch angles as reported above.

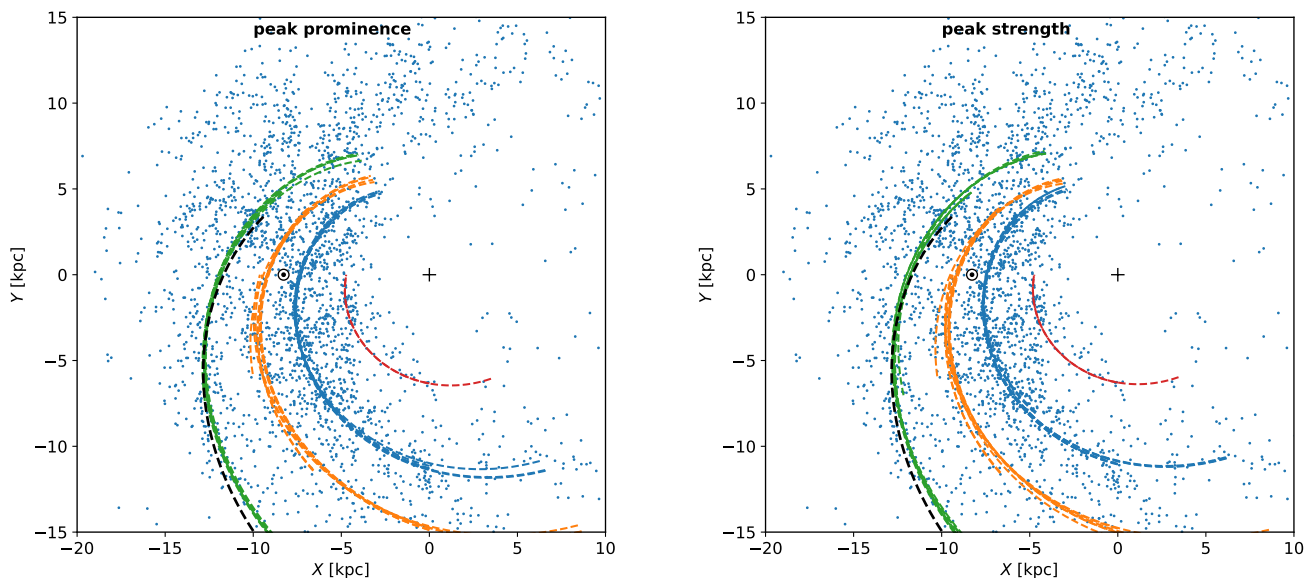
5. Discussion

In the previous section we derived spiral arm parameters over a suite of overlapping azimuth ranges (See Table 1.) Though the arm parameters for a given arm do not vary by a large amount, it raises the question of which set of parameters one should use for each arm. Given that the spiral structure in the Cepheid distribution is most clearly evident in the third and fourth quadrants, we suggest to use the set of arm parameters in the azimuth range $[-90^\circ, 0^\circ]$, where the pitch angles derived from both methods (strength or prominence) agree quite well for all the arms. Averaging the pitch angles and $\ln R_0$ from the two methods in this azimuth range results in the recommended spiral arm parameters given in Table 2.

As already noted in Section 3, the pitch angles of the arms increase as we move from the inner to the outer arms. This progression would apparently argue against these arms being part of a common grand design spiral pattern, since they do not share the

Table 1. Spiral arm parameters found for each arm over different azimuth ranges. N is the number of Cepheids found in the azimuth range, ϕ and the pitch angle θ are in degrees, and $\ln R_0$ is for R_0 in kpc.

ϕ range	N	Scutum				Sgr-Car				Orion				Perseus			
		strength		prominence		strength		prominence		strength		prominence		strength		prominence	
		θ	$\ln R_0$	θ	$\ln R_0$	θ	$\ln R_0$	θ	$\ln R_0$	θ	$\ln R_0$	θ	$\ln R_0$	θ	$\ln R_0$	θ	$\ln R_0$
[-120, 0]	1431	10.1	1.56	10.7	1.55	13.7	2.0	14.2	2.0	16.1	2.24	15.0	2.26	22.1	2.46	21.3	2.47
[-90, 0]	1331	10.2	1.56	10.6	1.55	14.5	2.0	14.8	2.0	16.0	2.24	15.6	2.25	22.0	2.46	20.9	2.48
[-120, 30]	2012	—	—	—	—	13.4	2.01	15.7	1.99	17.3	2.21	16.7	2.22	21.6	2.47	21.2	2.47
[-90, 30]	1912	—	—	—	—	14.3	2.0	15.5	1.99	17.5	2.21	17.0	2.22	21.5	2.47	20.9	2.47
[-60, 30]	1637	—	—	—	—	11.4	2.01	15.0	1.99	19.3	2.22	18.7	2.22	21.3	2.47	20.7	2.47
[-120, 60]	2422	—	—	—	—	13.6	2.01	15.7	1.99	17.9	2.2	16.9	2.21	20.2	2.48	20.8	2.48
[-90, 60]	2322	—	—	—	—	14.2	2.0	15.5	1.99	18.6	2.21	17.3	2.21	20.2	2.48	20.6	2.48
[-60, 60]	2047	—	—	—	—	12.1	2.01	15.0	2.0	19.7	2.22	19.1	2.22	20.0	2.48	20.3	2.48
[-30, 60]	1518	—	—	—	—	12.0	2.01	14.7	2.0	22.7	2.25	21.5	2.24	18.4	2.47	22.5	2.47


Fig. 8. The XY distribution of the dynamically young Cepheids with the arms from all considered azimuth ranges overplotted. Red corresponds to the Scutum arm, the blue curve to the Sagittarius-Carina arm, the gold curve the Local (Orion) arm, and the green the Perseus arm. The black dashed curve is an arm seen by Levine et al. (2006) in the HI.

same pitch angle. However, we cannot help but note that the logarithmic radial separation between the Scutum and Sgr-Car arms ($\Delta \ln R_0 = 0.44$) is almost the same as that between the Sgr-Car and Perseus arms (0.46). (Taking 0.45 as the $\Delta \ln R_0$ separation between a four arm spiral pattern would imply a pitch angle of about 16° .) While suggestive, conclusions drawn from these arm spacings can only be tentative, given that the detection of the Scutum arm is itself tentative and, even if it is a positive detection, its distance may be biased given the uncertainties in the extinction at this direction and distance.

Table 2. Recommended spiral arm parameters from the Cepheid distribution in the third and fourth quadrants. Pitch angle θ is in degrees, and $\ln R_0$ is for R_0 in kpc.

Arm	θ	$\ln R_0$
Scutum	10.4	1.56
Sgr-Car	14.7	2.0
Orion	15.8	2.25
Perseus	21.5	2.47

The most obvious spiral arm in the Cepheid distribution is the Sgr-Car arm in the fourth quadrant. For this arm we note that not only do we find consistent pitch angles for all azimuth ranges considered, but this arm also has a tangent in the first quadrant at $l \approx 50^\circ$, which has historically been associated with the Sagittarius arm. (For a detailed discussion of the history of the Sagittarius arm, see appendix A of Kuhn et al. (2021).) That is, whether we extrapolate the spiral arm derived from the Cepheids in the fourth galactic quadrant, or also use the Cepheids in the first quadrant, the nearest arm inside the solar circle has arm tangents that correspond to both the Carina arm (at $l \approx 285^\circ$) and the Sagittarius arm (at $l \approx 50^\circ$) suggesting that these two tangents are indeed from a single arm, traditionally recognized as the Sagittarius-Carina (Sgr-Car) arm.

The second most evident arm in the Cepheid distribution is the outermost Perseus arm in the third quadrant, which we find to coincide with one of the four arms seen by Levine et al. (2006) (their arm n. 2, see their Table 1 and Fig. 4A) in HI, shown in Fig. 8 as the black dashed curve, consistent with previous findings (Poggio et al. 2021; Gaia Collaboration et al. 2022). Ac-

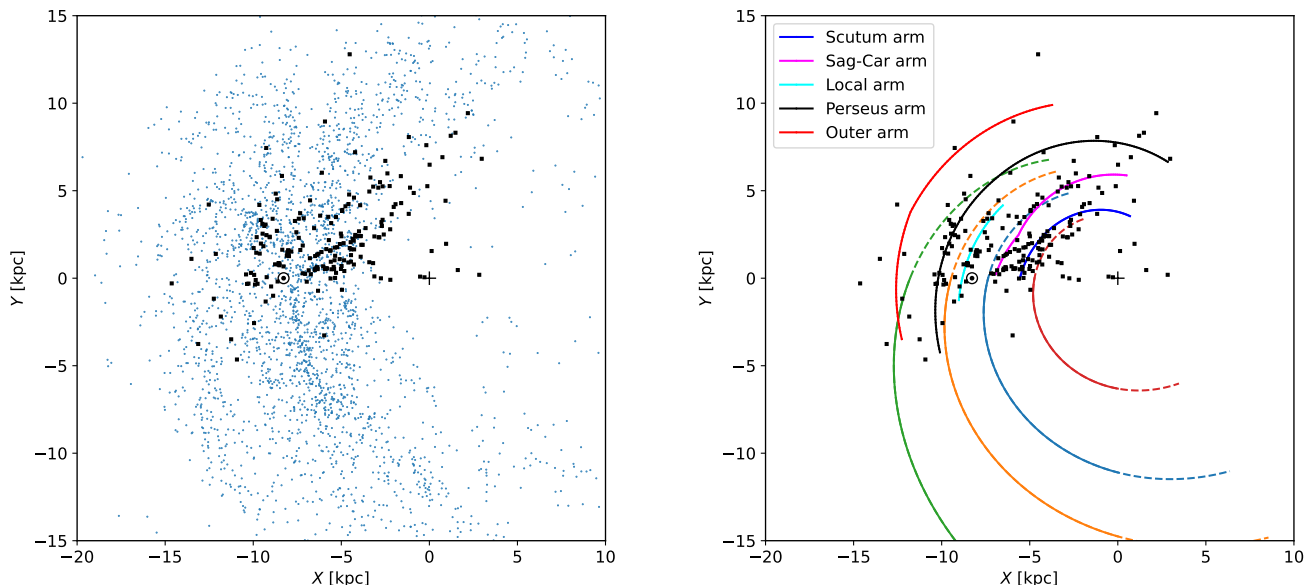


Fig. 9. Left panel: Comparison of the Cepheids sample (blue dots) with the masers from R19, shown as black squares. Right panel: Comparison between the model derived in this work (colors of the spiral arms are the same as in previous Figures) and the spiral arm model from R19.

According to their location, two other arms of Levine (their arm n. 3 and 4) coincide with the Local and Sagittarius arm in the fourth quadrant, but have significantly different orientations than those seen here in the Cepheids.

In contrast, the Local (Orion) arm is much weaker than either the Sgr-Car or the Perseus arm. Indeed, it may only be thanks to our favourable position with respect to this arm that we can detect it at all. Nevertheless, it is evident over a large range of azimuths, confirming that it is a real feature of significant length, as has been recently suggested in the literature (Xu et al. 2016, 2018; Poggio et al. 2021). However, these works suggest a slightly different orientation of the Local arm: Using *Gaia* DR2 data Xu et al. (2018) suggest that the Local arm continues into the fourth quadrant and bends inward toward the Galactic center. On the other hand, the Local arm from the overdensity maps of upper main sequence (OBA) stars from *Gaia* DR3 in Poggio et al. (2021) appears to be extending from the first to the third quadrant, with a more open geometry. This is in agreement with the orientation of the Local arm seen here in the Galactic Cepheids. In any case, judging from the distribution of the Cepheids, it is certainly not one of the major arms of the Milky Way though, while much weaker, it seems to be as long as the Sgr-Car arm.

It is worth comparing our results with other recent studies of Galactic spiral structure based on Cepheids. Bobylev (2022) used about 600 pre-selected Cepheids from Skowron et al. (2019a,b) to measure the pitch angle of the Sgr-Car arm and an outer arm beyond Perseus. Performing a linear least-squares fit in $\ln(R) - \phi$ space, they find similar pitch angles for both arms. For the Sgr-Car arm which is most clearly seen in their data set, they find a pitch angle near 12° . However their solution for each arm is already constrained by their pre-selection over a limited range in $\ln(R) - \phi$. In contrast, our methodology does not rely on pre-assigning Cepheids to specific arms, identified by the peaks in the distribution of the Cepheids in $\ln(R) - \phi$ space.

Lemasle et al. (2022) derive distances using MidIR Wesenheit magnitudes, which may still suffer from extinction effects, as discussed in Paper I. To identify spiral structure they used a t-SNE+HDBSCAN algorithm, feeding the HDBSCAN clustering algorithm (Campello et al. 2013) the output from the two-dimensional t-SNE (t-distributed Stochastic Neighbor Embedding, van der Maaten & Hinton (2008)), generated from providing the algorithm the $(\phi, \ln R)$ coordinates. Using primarily the subsample of Cepheids younger than 150 Myr, they identify numerous spiral arm segments. However they note, "that the algorithm is sensitive to small gaps (regions without stars) in individual spiral arms. A given spiral arm may then be split in several segments limited by those gaps." Indeed, they find about 18 spiral segments. This result should not be interpreted as evidence that the Milky Way is flocculent: Spiral arms on kiloparsec scales are not continuous structures, but are a perceived pattern on large scales made up of spurs, feathers and large, disconnected, star formation regions. In addition, extinction effects can introduce additional apparent gaps that are not real. For these reasons we apply the logarithmic spiral formalism only to datasets covering a large range ($\Delta\phi \geq 90^\circ$) in Galactic azimuth, to map the spiral structure on a large-scale.

Until now the most constraining data for the large-scale structure of the spiral arms has been the masers found in high mass star forming regions (Reid et al. 2019, hereafter R19). The Sgr-Car arm is identified with the well identified tangent at $l \approx 283^\circ$ (Bronfman et al. 2000). Using this tangent, together with masers in the first quadrant, R19 fit a log-periodic spiral, allowing for a "kink" in the arm, with different pitch angles on either side of the kink. In this way R19 connects both arm tangents to construct the Sgr-Car arm, obtaining a pitch angle of $17.1 \pm 1.6^\circ$ after the kink (i.e. towards the fourth quadrant), and a pitch angle of $1.0 \pm 2.1^\circ$ before the kink (i.e. in the direction of Galactic rotation). However, for the Cepheids we find that the Sgr-Car arm geometry that we deduce from the Cepheids, with a pitch angle of about 15° , is able to account for both arm tan-

gents without the need of a kink or additional constraints, and also passes through the masers that are located in the direction of the arm tangent at $l \approx 50^\circ$.

While the large-scale Cepheid distribution seems to support the geometry of the Sgr-Car arm that is traditionally assumed, we note that the position of Sgr-Car kink employed by R19 roughly corresponds with a gap observed in the maser's distribution, which we also see in the Cepheid distribution. Kuhn et al. (2021) identify 25 star-forming regions in the galactic longitude range $l \approx 4.0^\circ - 18.5^\circ$ arranged in a long linear structure with a high pitch angle of 56° . We observe a similar structure in our Cepheid sample, and note that it is also present in the maser distribution. One possible interpretation is that this high-pitch angle structure is a spur that departs from the Sgr-Car arm. Indeed, if we inspect external spiral galaxies, it is not rare to see spurs (luminous features) and feathers (dust features) that extend from spiral arms to inter-arm regions. An alternative interpretation is that this high-pitch angle structure represents the main spiral arm itself, so that the arm has an abrupt change in pitch angle in the first quadrant. In this scenario, the gap in the stellar distribution observed in the Cepheids and masers would represent an inter-arm region, and the two tangents at $l \approx 285^\circ$ and $l \approx 50^\circ$ would not be part of the same arm.

In the inner regions, there is a small azimuthal range which is covered by both our model and the R19 model for the Scutum arm. As we can see from Fig. 9 (right panel), the Scutum arm derived here has a very similar pitch angle to the one from R19, but slightly shifted toward the inner parts of the Galaxy. The Orion (Local) arm in the Cepheids agrees well with that seen in the masers, though we find a somewhat larger pitch angle than that derived by R19 (11.4°).

In contrast with the other arms, the orientation of the Perseus arm in the two models is totally different. As already mentioned, the geometry of this arm in the Cepheids agrees quite well with an arm seen in HI as well as young upper-mainsequence stars in the third quadrant. Accepting the R19 mapping of the Perseus arm in the second quadrant, we must conclude that either the Perseus arm has an abrupt change in pitch angle, or the Cassiopeia region is the end of the Perseus arm and a different set of arms dominate the outer disk, with the Cassiopeia star formation region being where these two arms intersect.

If we just consider the source distribution and ignore the models, we observe that the positions of Cepheids and masers in the Cassiopeia region (the overdensity at $l \approx 110 - 140^\circ$) do not perfectly coincide: the masers are slightly shifted toward lower Galactocentric radii compared to the distribution of Cepheids. Based on the distance determinations obtained in Paper I and this work, we conclude that such a shift is not due to distance errors. Offsets between the distribution of masers and Cepheids, seen here in the Perseus arm and also the Scutum arm, could be explained by the age difference between the two populations and the difference between the angular pattern speed of the arm and angular rotation rate of the stars: Maser emission originates from circumstellar material around high mass stars, so expected to be very young, while our selected Cepheids are older (see Fig. 1) and so have had time to move away from their birthplaces, therefore the spiral structure they form may be different than the one formed by masers (see Fig. 3 in Skowron et al. 2019a). However, the offset seen for the Perseus arm would require this section of the arm to be inside its corotation, while the offset seen in the Scutum arm would require the Cepheids in this arm to be outside its corotation.

While part of the observed differences between the Cepheid distribution and the masers might be real and physically moti-

ated, it is important to note that the comparison between our results and the R19 model strongly depends on the criteria adopted to assign each maser to a spiral arm. For instance, if the nearby masers at $l \approx 180^\circ$ were assigned to the Local arm, instead of being assigned to the Perseus arm (as done in R19), the resulting geometry of the Perseus and Local arms would be different, and presumably more in agreement with the one obtained here.

6. Conclusions

In this contribution we have mapped the large-scale spiral structure of the Galaxy with dynamically young Cepheids, using new distance estimates based on midIR photometry from an accompanying paper (see Paper I), and a new age criteria. Our method for deriving spiral arm parameters does not rely on pre-assigning sources to specific arms, but instead detects and derives arm parameters based on the overall distribution of Cepheids over a large range in galactic azimuth. Our approach is informed by the understanding that the logarithmic spiral originates as an empirically motivated geometrical model to describe the morphology of disk galaxies on large scales, and that spiral arms are composed of a rich variety of discontinuous substructure on the kiloparsec scale that are often not well described by a logarithmic spiral. In addition, for our own Galaxy we have the additional difficulty that we do not have an external global view of the disk, but our samples of spiral tracers are unavoidably incomplete and limited by extinction that will introduce additional gaps in our knowledge of the true distribution of sources. For the Cepheids this is especially an issue in the parts of the first quadrant that do not fall within the OGLE footprint. Nevertheless the Cepheids make an excellent tracer of the young stellar population.

It is important to note that our source list is from a compilation of various surveys (Pietrukowicz et al. 2021), differing in their on-sky footprint, their cadence, photometric bands, magnitude limit, etc. (See Fig. 2 of Paper I.) Naturally, this introduces inhomogeneity in our sampling of the number of Cepheids across the sky. In the future Cepheids will continue to be employed to investigate Galactic structure on large scales, as has been done in the past. For example, Cepheids have also been used to study the shape of the warp (Skowron et al. 2019a,b; Chen et al. 2019) and its associated kinematics (Poggio et al. 2018; Dehnen et al. 2023; Hranar Jónsson & McMillan 2024). To take full advantage of the large scale coverage provided by the Cepheids will require modelling such an incomplete and inhomogeneous data set. One will need to take into account both extinction and the selection function, i.e., the expectation of the fraction of Cepheids that is in one's dataset as a function of observables (ex: $l, b, G, G-Rp$ and other quantities), to properly infer the intrinsic properties of the population (Khanna et al. in prep., Cantat-Gaudin et al. 2023, 2024).

The clearest and most prominent arm seen in our dataset, and which is immediately visible in both the XY and $\phi' - \ln R$ plots, is the Sagittarius-Carina (Sgr-Car) arm. The spiral arm parameters derived for this arm naturally accounts for both tangent directions that have been traditionally attributed to the Sgr-Car arm. The second most obvious spiral feature, seen in the third quadrant, is one we identify with the Perseus arm, given that this spiral arm goes through the large Cassiopeia star forming region long identified as the nearest segment of the Perseus arm. However, consistent with earlier works, we find that this arm has a significantly larger pitch angle than that derived from the masers in the second quadrant.

Being intrinsically bright, the Cepheids allow us to map young stellar populations over a considerable extent of the

Galaxy, and make an excellent complimentary dataset to the masers, providing us with information in the third and fourth quadrants where, to date, there are still few masers with astrometric parallaxes, while in the first and second quadrants the masers are less hindered by extinction effects than the Cepheids, which can only be reliably identified in the optical. Thanks to these two populations and future surveys, we can only look forward to the large-scale structure of our Galaxy being more fully revealed, as additional maser parallaxes become available from the VLBI measurements in the southern hemisphere, and as deep all-sky multi-epoch photometric surveys allow us to identify Cepheids currently hidden by interstellar extinction.

Acknowledgements. We thank Alessandro Spagna and Robert Benjamin for useful discussions. RD and EP are supported in part by the Italian Space Agency (ASI) through contract 2018-24-HH.0 and its addendum 2018-24-HH.1-2022 to the National Institute for Astrophysics (INAF). SK and RD acknowledge support from the European Union's Horizon 2020 research and innovation program under grant agreement No 101004110. DMS acknowledges support from the European Union (ERC, LSP-MIST, 101040160). Views and opinions expressed are however those of the authors only and do not necessarily reflect those of the European Union or the European Research Council. Neither the European Union nor the granting authority can be held responsible for them. SK acknowledges use of the INAF PLEIADI@IRA computing resources (<http://www.pleiadi.inaf.it>). This work presents results from the European Space Agency (ESA) space mission Gaia. Gaia data are being processed by the Gaia Data Processing and Analysis Consortium (DPAC). Funding for the DPAC is provided by national institutions, in particular the institutions participating in the Gaia MultiLateral Agreement (MLA). The Gaia mission website is <https://www.cosmos.esa.int/gaia>. The Gaia archive website is <https://archives.esac.esa.int/gaia>. This publication makes use of AllWISE data products derived from the Wide-field Infrared Survey Explorer, which is a joint project of the University of California, Los Angeles, and the Jet Propulsion Laboratory/California Institute of Technology, and NEOWISE, which is a project of the Jet Propulsion Laboratory/California Institute of Technology. WISE and NEOWISE are funded by the National Aeronautics and Space Administration. This work has used the following software products: Matplotlib (Hunter 2007); Astropy (Astropy Collaboration et al. 2018); SciPy (Virtanen et al. 2020); and NumPy (Harris et al. 2020). This project was developed in part at the Lorentz Center workshop "Mapping the Milky Way", held 6-10 February, 2023 in Leiden, Netherlands.

References

- Anders, F., Padois, C., Vilanova Sar, M., et al. 2024, arXiv e-prints, arXiv:2406.06228
- Anderson, R. I., Saio, H., Ekström, S., Georgy, C., & Meynet, G. 2016, *A&A*, 591, A8
- Astropy Collaboration, Price-Whelan, A., Sipőcz, B. M., et al. 2018, *AJ*, 156, 123
- Bobylev, V. V. 2022, *Astronomy Letters*, 48, 126
- Bono, G., Braga, V. F., & Pietrinferni, A. 2024, *A&A Rev.*, 32, 4
- Bronfman, L., Casassus, S., May, J., & Nyman, L. Å. 2000, *A&A*, 358, 521
- Campello, R. J. G. B., Moulavi, D., & Sander, J. 2013, in *Advances in Knowledge Discovery and Data Mining*, ed. J. Pei, V. S. Tseng, L. Cao, H. Motoda, & G. Xu (Berlin, Heidelberg: Springer Berlin Heidelberg), 160–172
- Cantat-Gaudin, T., Fouesneau, M., Rix, H.-W., et al. 2023, *A&A*, 669, A55
- Cantat-Gaudin, T., Fouesneau, M., Rix, H.-W., et al. 2024, *A&A*, 683, A128
- Chen, X., Wang, S., Deng, L., et al. 2019, *Nature Astronomy*, 3, 320
- Cutri, R. M., Wright, E. L., Conrow, T., et al. 2013, Explanatory Supplement to the AllWISE Data Release Products, Explanatory Supplement to the AllWISE Data Release Products, by R. M. Cutri et al.
- Dehnen, W., Semiczuk, M., & Schönrich, R. 2023, *MNRAS*, 523, 1556
- Drimmel, R., Khanna, S., D'Onghia, E., et al. 2023, *A&A*, 670, A10
- Gaia Collaboration, Drimmel, R., Romero-Gomez, M., et al. 2022, arXiv e-prints, arXiv:2206.06207
- GRAVITY Collaboration, Abuter, R., Aymar, N., et al. 2022, *A&A*, 657, L12
- Griv, E., Jiang, I.-G., & Hou, L.-G. 2017, *ApJ*, 844, 118
- Haffner, L. M., Reynolds, R. J., & Tufte, S. L. 1999, *ApJ*, 523, 223
- Harris, C. R., Millman, K. J., van der Walt, S. J., et al. 2020, *Array programming with NumPy*
- Hrannar Jónsson, V. & McMillan, P. J. 2024, arXiv e-prints, arXiv:2405.09624
- Hunter, J. D. 2007, *Computing In Science & Engineering*, 9, 90
- Kuhn, M. A., Benjamin, R. A., Zucker, C., et al. 2021, *A&A*, 651, L10
- Lemasle, B., Lala, H. N., Kovtyukh, V., et al. 2022, *A&A*, 668, A40
- Levine, E. S., Blitz, L., & Heiles, C. 2006, *Science*, 312, 1773
- Minniti, J. H., Zoccali, M., Rojas-Arriagada, A., et al. 2021, *A&A*, 654, A138
- Morgan, W. W., Whitford, A. E., & Code, A. D. 1953, *ApJ*, 118, 318
- Pedregosa, F., Varoquaux, G., Gramfort, A., et al. 2011, *Journal of Machine Learning Research*, 12, 2825
- Pietrukowicz, P., Soszyński, I., & Udalski, A. 2021, *Acta Astron.*, 71, 205
- Poggio, E., Drimmel, R., Cantat-Gaudin, T., et al. 2021, *A&A*, 651, A104
- Poggio, E., Drimmel, R., Lattanzi, M. G., et al. 2018, *MNRAS*, 481, L21
- Reid, M. J., Menten, K. M., Brunthaler, A., et al. 2019, *ApJ*, 885, 131
- Schlafly, E. F., Meisner, A. M., & Green, G. M. 2019, *ApJS*, 240, 30
- Skowron, D. M., Skowron, J., Mróz, P., et al. 2019a, *Science*, 365, 478
- Skowron, D. M., Skowron, J., Mróz, P., et al. 2019b, *Acta Astron.*, 69, 305
- van de Hulst, H. C., Muller, C. A., & Oort, J. H. 1954, *Bull. Astron. Inst. Netherlands*, 12, 117
- van der Maaten, L. & Hinton, G. 2008, *Journal of Machine Learning Research*, 9, 2579
- VERA Collaboration, Hirota, T., Nagayama, T., et al. 2020, *PASJ*, 72, 50
- Virtanen, P., Gommers, R., Oliphant, T. E., et al. 2020, *SciPy 1.0: Fundamental Algorithms for Scientific Computing in Python*
- Wright, E. L., Eisenhardt, P. R. M., Mainzer, A. K., et al. 2010, *AJ*, 140, 1868
- Xu, Y., Bian, S. B., Reid, M. J., et al. 2018, *A&A*, 616, L15
- Xu, Y., Hao, C. J., Liu, D. J., et al. 2023, *ApJ*, 947, 54
- Xu, Y., Reid, M., Dame, T., et al. 2016, *Science Advances*, 2, e1600878
- Zari, E., Rix, H. W., Frankel, N., et al. 2021, *A&A*, 650, A112